Analyst

PAPER

View Article Online
View Journal | View Issue

Cite this: *Analyst*, 2026, **151**, 1467

Characterizing microscopic calcification deposits on acrylic intraocular lenses

Cassandra L. Ward, *[a] S. Sameera Perera,[a] Zhi Mei,[a] Bing X. Ross,[b] Manisha De Alwis Goonatilleke,[c] Mahdi Ayoubi,[c] Yao Xiao,[d] Andrew P. Ault,[d] Judy A. Westrick,[a] Thomas H. Linz[e] and Xihui Lin[b]

Intraocular lenses (IOLs) are implanted into the eyes during cataract surgery to improve vision. A rare complication following IOL implantation is the formation of crystallized deposits on the lenses, which significantly impair vision, necessitating subsequent surgical IOL exchange. Preventing these deposits from forming is critical, but this requires definitive molecular assignments of the crystals and knowledge of their mechanism of formation. Determining this information presents a significant analytical challenge due to the low numbers of crystals and curvature of the IOLs that limit use of conventional methods. Here, we report the development of multiple complementary analytical methods to characterize IOLs explanted from human patients and attain insight into the chemical identity and mechanism of the deposits. Initial elemental analyses using energy-dispersive X-ray spectroscopy (EDS) and X-ray photoelectron spectroscopy (XPS) revealed that IOL crystals contained calcium, phosphorus, and sodium and provided quantitative ratios between elements. Subsequent Raman spectroscopy identified carbonate in the crystals as well. An innovative single-crystal X-ray diffraction (XRD) method with integrated Rietveld analysis was then developed, which conclusively determined that IOL crystals were composed of substituted hydroxyapatite. Collectively, the data obtained from EDS, XPS, XRD, and Raman indicate that IOL deposits are composed of crystalline $Ca_9Na(PO_4)_5(CO_3)(OH)_2$ layered with amorphous calcium phosphate. This structure is similar to bone, suggesting that a similar ossification mechanism is followed. The robust analytical methods developed herein provide the most comprehensive characterization of IOL crystals to date and signify that the microenvironment of the eye is conducive to bone mineralization pathways that induce crystal formation on IOLs.

Received 18th September 2025,
Accepted 31st January 2026

DOI: 10.1039/d5an00999e

rsc.li/analyst

Introduction

The formation of crystallized deposits on intraocular lenses (IOLs) is a rare but serious complication after cataract surgery.[1,2] Accumulation of these crystals causes progressive vision deterioration and visually significant glare, which necessitates surgical exchange of the IOLs. Repeated surgical procedures on the eyes risk complications including retinal detachment, high intraocular pressure, and cystoid macular edema that further jeopardize patient's vision.[3–5] Preventing these deposits from first taking root is essential, but this requires knowledge of how they arise. Previous studies suggested that manufacturing defects in the lens material are responsible for crystal formation.[3,6–8] IOLs are commonly made of hydrophilic acrylic polymers (*e.g.* poly(2-hydroxyethyl methacrylate)) because of their biocompatibility and foldability to facilitate implantation.[9,10] Given the low rate of occurrence of IOL crystals, it is plausible that uncommon manufacturing issues can leave voids in which seed crystals can grow. However, it is also imperative to determine the composition of IOL deposits. Identifying the molecular structure of the crystals and elucidating their mechanism of growth will provide insight into how to prevent their occurrence.

Previous studies used scanning electron microscopy (SEM) with energy dispersive X-ray spectroscopy (EDS) to determine the chemical formula of the small deposits (<100 μm diameter) on IOLs. These elemental analyses revealed that IOL crystals contain calcium and phosphorous, and were reported to be either hydroxyapatite (HAP, $Ca_{10}(PO_4)_6(OH)_2$) or octacalcium phosphate (OCP, $Ca_8(PO_4)_4(HPO_4)_2$),[11–13] with one report suggesting sodium-substituted HAP with an additional Zn-containing phase.[14] HAP is a well-known calcium phosphate found

[a]*Lumigen Instrument Center, Wayne State University, 5101 Cass Ave, Detroit, Michigan 48202, USA. E-mail: ward@wayne.edu; Tel: +1 313-577-2587*
[b]*Kresge Eye Institute/Department of Ophthalmology, Visual and Anatomical Sciences, Wayne State University School of Medicine, Detroit, Michigan 48201, USA*
[c]*Thermo Fisher Scientific, Hillsboro, Oregon 97124, USA*
[d]*Department of Chemistry, University of Michigan, Ann Arbor, Michigan 48109, USA*
[e]*Department of Chemistry, Wayne State University, Detroit, Michigan 48202, USA*

in biological systems and is the primary material of bones and teeth. OCP is a metastable precursor of HAP and is involved in the bone mineralization pathway.[15,16] Given their precedence in biology,[17–21] HAP and OCP are plausible materials for IOL deposits. However, the molecular assignments in previous reports are tenuous. HAP and OCP are similar in composition, which presents an analytical challenge when trying to distinguish them. Reports claiming to distinguish HAP and OCP by SEM relied on morphology differences between crystals.[11,12] However, this approach has the potential for bias because the growth mechanism of crystals influences their morphology, and synthetic crystal standards do not grow identically to biological IOL crystals. EDS is a better alternative because of its ability to calculate the ratio of Ca/P, which can distinguish different phases of calcium phosphate (1.33 for OCP; 1.67 for HAP). However, most previous reports only identified the elements present with EDS and did not quantify the Ca/P ratio of IOL crystals.[7,22–24] These issues highlight the need for more thorough quantitative characterizations of IOL deposits to definitively identify their composition.

Other common analytical techniques are incapable of providing conclusive molecular assignments for IOL crystals. HAP and OCP both have identical functional groups which give rise to spectrally similar features when characterized by Raman spectroscopy, infrared spectroscopy (IR), and X-ray photoelectron spectroscopy (XPS).[25,26] The best alternative to distinguish HAP and OCP is X-ray diffraction (XRD) because of its aptitude to differentiate different crystalline structures with the same chemical formula. Specifically, powder XRD is a logical technique to analyze IOLs because their deposits consist of numerous randomly oriented crystals which collectively form a powder sample. Although powder XRD can distinguish different calcium phosphates,[25] standard powder diffractometers cannot analyze IOLs due to the low number of crystals present and the small sizes of the lenses.[26] Single-crystal diffractometers (SCDs) overcome these limitations but are not historically used for powder measurements because of poor resolution between peaks and low intensities at high angles due to beam divergence and large step sizes between data points (>0.02°). However, the sources and optics of SCDs have improved in recent years to better collimate the X-ray beam and increase their power output. Additionally, step sizes have been enhanced to provide comparable measurements as those from powder diffractometers. The technical advancements in SCDs may provide adequate performance to analyze crystals on IOLs.

This report describes the development of multi-faceted analytical methods to characterize IOLs explanted from patients to identify the crystalline material and determine a potential mechanism for its formation. SEM images showed that deposits formed on both the surface and within the IOL. Milling the IOL with a focused ion beam (FIB)/SEM revealed that the deposits damaged the polymer but that no obvious manufacturing defects were present prior to crystal formation. Powder XRD was collected using a SCD to determine the chemical composition and structure of the deposits. The low 2θ angles measured by the SCD enabled definitive identification of IOL crystals as HAP, as opposed to OCP. Further spectroscopic characterizations were then performed to identify potential atomic substitutions in the IOL HAP crystals. EDS revealed the presence of Na in the crystals while Raman microscopy and XRD identified carbonate. The combination of spectroscopic and diffraction results along with Rietveld structural analysis collectively converged on IOL crystals being comprised of sodiated B-type carbonated HAP ($Ca_9Na(PO_4)_5CO_3(OH)_2$) interspersed with amorphous calcium phosphate. Only by employing multiple complementary analytical techniques were the identity of IOL deposits obtained. The proposed substituted HAP structure is similar to the layered crystals found in bone and teeth, suggesting that IOL deposits are formed *via* a similar biological mechanism.

Materials and methods

HAP powder was purchased from Sigma-Aldrich, Co. (synthetic, 99.8% trace metals basis (excludes Mg), St Louis, MO) and OCP was purchased from AA Blocks Inc. (Phosphoric acid, calcium salt, 3 : 4, 98% San Diego, CA) and were analyzed without further purification. Parabar 10312 oil was obtained from Hampton Research (Aliso Viejo, CA).

This study was approved by the Institutional Review Board at Wayne State University, United States. Informed consent was obtained from patients who required surgical exchange of their IOLs. Hydrophilic Bausch & Lomb (models MI60L or AO60) IOLs were removed from six patients. Five of these IOLs contained crystal deposits, and one was used as an explanted control. After removal from the eye, the IOLs were immediately submerged in a balanced saline solution. An additional control IOL that had not been implanted in a patient was also included in the study. Patient IOLs were removed due to significant loss in vision, which upon physical examination, deposits were identified as the cause. The explanted control lens was removed due to other medical complications of the patient and not due to deposits. The intraocular times of the IOLs ranged from 3.5–8.5 years (Table 1). The formation of deposits likely stemmed from numerous factors including patient comorbidities. Large-scale clinical investigations are needed to identify critical risk factors, which is beyond the scope of this study focused on developing analytical characterizations.

The explanted IOLs were examined under a Wild M5 or Leica M205 stereomicroscope to observe the distribution of deposits. Micrographs of the lenses were captured using a Canon EOSi7 or Leica K5C camera, respectively. The morphology of the surface and cross-section of the explanted and control IOLs were examined using a field emission SEM (JEOL JSM 7600F; Peabody, MA). A razor blade was used to cut the IOLs for cross-sectional analysis of the optic area. The samples were coated with gold using a sputter coater (Ernest F. Fullam Inc.; Latham, NY). The composition of the deposits was determined by EDS. Because the samples were coated in gold, all EDS results show a peak for gold, which is excluded in the relative atomic percentages (ZAF matrix correction). The accelerat-

Table 1 List of the different Bausch & Lomb IOLs analyzed in this study. Lenses 1–6 were explanted from patients. Lens 7 is a non-implanted control. Crystal locations, sizes, and coverage are specified for each IOL sample

Lens number	Model	Crystal locations	Presence of subsurface crystals	Approx. crystal size	Approx. crystal coverage	IOL intraocular time (years)
1	MI60L	Optic and haptic	No	30–100 μm	90%	6.6
2	AO60	Optic and haptic	Yes	15–40 μm	50%	3.5
3	MI60L	Optic	Yes	7–15 μm	40%	7.8
4	AO60	Optic and haptic	Yes	50–125 μm	18%	8.5
5	MI60L	Optic	Yes	10–30 μm	4%	3.9
6	AO60	NA	NA	NA	0%	4.0
7 (Control)	MI60L	NA	NA	NA	0%	0

ing voltage for EDS was kept below 6 keV to reduce degradation of the crystals and lens material. This reduced accelerating voltage also improves the precision of the EDS measurements.[27] Analyses were also conducted at a higher accelerating voltage to search for Zn, which was not found (data not shown). FIB/SEM was used to collect 3D images of the subsurface crystals to calculate the sample porosity using a Thermo Fisher Scientific Helios 5 UX (Hillsboro, Oregon). The samples were first carbon coated for imaging, and then a tungsten protective cap was used before milling. The Ga^+ ion beam (30 kV, 2.6 nA) consumed 50.0 × 26.4 × 10.1 μm. A total of 500 images, 20 nm thick, were imaged using a concentric backscatter detector. These 2D images were reconstructed using Avizo (version 2024.2, Thermo Fisher Scientific) to generate a 3D image. Using Avizo, the volume fraction of crystals and pores was calculated with the remaining volume fraction assigned as the IOL polymer.

X-ray photoelectron spectroscopy (XPS) data were collected with a Thermo Fisher Scientific Nexsa XPS system equipped with a hemispherical analyzer and monochromatic Al Kα source (spot size ~400 μm^2). One IOL with deposits (Lens 1) was dried in a vacuum desiccator for approximately 12 h to remove any surface moisture. The dried sample was mounted using conductive Cu tape and held under vacuum (<6×10^{-7} mbar) in the entry-lock chamber for ~30 min. The base pressure of the analysis chamber during the experiment was ~2.5×10^{-7} mbar. The spectrometer was calibrated using a pristine gold (Au $4f_{7/2}$ at 84.0 eV) standard. A flood gun was employed to neutralize surface charges. C 1s signal from adventitious carbon as a binding energy standard at 284.8 eV was used to correct for charging.[28] Binding energy positions and Ca/P ratios of the crystal deposits were determined from high-resolution XPS core scans using 50 eV pass-energy, 100 ms dwell time, 0.1 eV energy step size, and five scans. Relative sensitivity factors provided within Avantage software (Thermo Fisher Scientific) were used to normalize peak intensities. Data was exported into CasaXPS software[29] for quantitative analysis of Ca/P ratios.

Powder XRD of the crystal deposits were collected under ambient conditions on a Bruker D8 Venture SCD using Cu Kα radiation (Incoatec IμS micro-focus source) with a 0.2 mm collimator. The diffractometer was equipped with a Photon III CPAD area detector. The IOLs were cut to approximately 300 μm × 300 μm × 200 μm under a stereomicroscope and were mounted on a micromount loop (MiTeGen, Ithaca, NY) using Parabar oil. Three Phi 360° scans were collected up to 120° 2θ (2θ = 25, 60, and 95° with Ω = 40°, Φ = 0°, χ = 0°, and detector distance of 100 mm) in transmission geometry. Total collection times were 30 min for each IOL or powder sample. The scans collected were then integrated using APEX4 (Bruker; Billerica, MA) Integrate Debye Rings module. The Powder Diffraction Files (PDF) database (International Centre for Diffraction Data; Newton Square, PA) was used to compare against the measured IOL powder patterns using EVA 4.0 (Bruker, Billerica, MA).

Raman spectroscopy was performed on the deposits using a Horiba LabRam Evolution Raman microscope system equipped with a 50 mW 532 nm Nd:YAG laser as the excitation source and an 1800 groove per mm diffraction grating. Images were acquired using the built-in confocal optical microscope (Olympus; Bartlett, TN). The following are additional instrument settings: 100× lens, 0.9 N.A. objective, slit 100, hole 400, ND filter 50%, and 15 s integration time. The resolution was calculated to be 0.7 cm^{-1}.

Results and discussion

Crystal morphology, localization, and elemental information using microscopy, EDS, and XPS

Late postoperative opacification is a serious complication with hydrophilic IOLs,[6,30] so multiple complementary methods were developed to characterize crystal deposits on IOLs to identify the material and obtain insight into its mechanism of formation. This study analyzed six lenses explanted from patients (Table 1). Five of the lenses were covered with crystals (Lenses 1–5) while the other lens did not have crystals (Lens 6). An additional non-implanted lens (Lens 7) was also analyzed as a control. All lenses were hydrophilic acrylic IOLs from Bausch & Lomb, but two models were studied, MI60L and AO60.

First, the explanted IOLs were examined by light microscopy. Of the five IOLs with crystals, all had deposits located on the optic region of the lens, and Lenses 1, 2, and 4 also had deposits on the haptic region (Fig. 1 and S1A–S4A). The distribution and extent of crystal coverage was different between lenses (Table 1); however, they all resulted in vision impairment for the patients, which necessitated explantation

and replacement of the IOLs. Interestingly, no correlations were observed between the intraocular time in the patient and the surface coverage or deposit location. SEM with EDS was then conducted to characterize the crystals on the surface of IOLs and determine if deposits also propagated into the lens subsurface. High-resolution SEM images showed that crystals formed in a disk shape (Fig. 2A and S1B–S4B), ranging from 7–125 μm in diameter. Closer examination of their morphology revealed that the disks are composed of concentric rings, which suggests crystal growth occurred in layers around a central nucleation point. This concentric ring profile is consistent with previous examinations of IOL deposits,[22] and is also similar to the structure of bone osteons.[31] The similar profile between bones and IOL crystals suggests a similar growth mechanism may cause crystal growth on IOLs,[32,33] which will be discussed further in later sections.

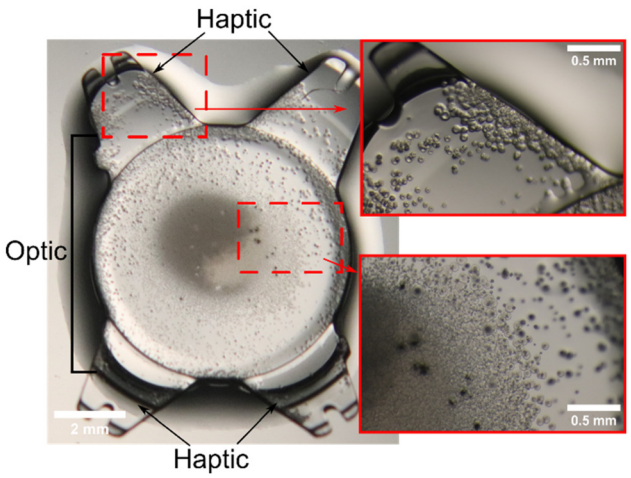

Fig. 1 Microscope image of explanted Lens 1 showing the crystallized deposits. The insets depict magnified areas of the haptic (top) and optic (bottom) regions of the IOL.

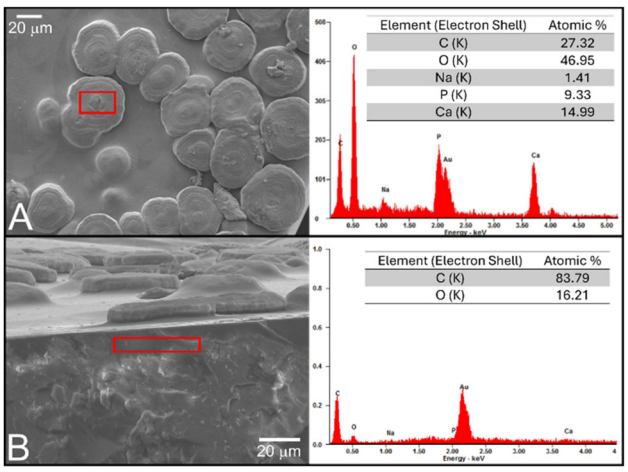

Fig. 2 SEM images of Lens 1 alongside EDS elemental analysis from the red highlighted regions. Crystal deposits were characterized on the (A) surface and (B) inside cross-section of the IOL. Surface crystals contained calcium, phosphorous, and sodium, but these elements were not observed in the subsurface, indicating no crystalline material was present below the surface. The gold observed in EDS data is from the gold coating, as explained in the Methods section.

EDS was used to evaluate the elemental composition of crystal deposits on both the surface and subsurface of the IOLs. The surface crystals of Lens 1 consisted of carbon (C), oxygen (O), calcium (Ca), phosphorus (P), and sodium (Na) (Fig. 2A). Analysis of the lens material away from the crystals revealed only C and O elements from the acrylic polymer of the lens. The same results were found from the other IOLs (Fig. S1B–S4B). These findings align with previous reports that IOL deposits are calcified crystals containing Ca and P. For Lens 1, only C and O were detected subsurface (Fig. 2B), while other lenses had crystals containing Ca, P, and Na below the surface (Fig. S1–S4). This discrepancy indicates that crystal penetration beneath the lens surface varies between patients.

While EDS successfully identified elements in the IOL deposits, it could not determine the molecular formula of the crystals because the measured relative atomic percentages contained signal from both the crystals and the lens polymer. As both materials contained C and O, precise molecular assignments could not be made. However, tentative assignments were possible using the relative atomic ratios of the inorganic elements. Based on previous reports of calcified IOLs, the crystals were expected to be either HAP (Ca/P = 1.67) or OCP (Ca/P = 1.33).[11,12] The average ratio of Ca/P in our study was 1.51 ± 0.14 from the five IOLs (n = 11). To validate these ambiguous results, the IOL samples were also analyzed with XPS (described in the SI section Ca/P ratio using XPS, Fig. S5, Table S1). Similar results were obtained for the Ca/P ratio, which was found to be 1.53 ± 0.09. Although both EDS and XPS produced statistically similar values, neither matched the expected values of HAP or OCP. This ambiguity suggests several options: the IOL crystals are comprised of a mixture of materials; IOL crystals are a different material than previously reported; or that elemental substitutions are present in the crystal lattice that altered the measured ratio.

The average Ca/Na ratio measured was 10 ± 2 (n = 8) from both top-down and cross-sectional crystals. While this could suggest that Na is present within the lens crystals, it could also be an artifact of residual NaCl from the eye or lens storage solution because both contain high concentrations of NaCl. However, EDS results did not indicate the presence of Cl on the IOLs, meaning that NaCl was not the source of the Na. Additionally, Na was not found in the lens material itself; only C and O were present, meaning that Na was only within the crystal deposits. Furthermore, NaCl is discernable on SEM images, and no obvious dried deposits were present after washing the IOLs. Collectively, these results indicate that Na is incorporated within the crystals on the five lenses. This finding is interesting because neither HAP nor OCP contain Na, further supporting our suggestion that previously reported compositions of IOL crystals are inaccurate.

Porosity of IOLs using FIB/SEM

The rare occurrence of opacification on IOLs has led to speculation that sporadic manufacturing defects—including porous voids within the IOL polymer—may create sites for crystals to form in a small fraction of lenses.[6–8] Although our study only had six IOLs explanted from patients, we sought to conduct a cursory evaluation to determine whether defects in the lens may have caused deposits to form. SEM cross-sectional images for Lenses 2–5 showed crystals in the subsurface, with Lenses 2, 4, and 5 also having what appear to be porous channels within the IOLs (Fig. S1C, S3C, S4C, and S4D). Subsurface crystals were significantly smaller than those on the surface—ranging from 1–10 μm in diameter—and EDS confirmed these crystals and pores contained Ca and P (Fig. S1C, S3C, and S4D). These results indicate that crystals can form beneath the surface of the lens and extend into the bulk polymer. Lens 3 had crystals that only formed in the subsurface in one region of the IOL without surface crystals (Fig. S6). These findings suggest that micro-sized voids may exist in the polymer material that serve as crystal nucleation sites, as opposed to crystals forming solely on the surface and then propagating into the lens to cause damage.

To determine whether voids or porous channels were present in the lenses before crystal deposits formed, Lenses 4 and 6 were further characterized using high-precision FIB/SEM. Both IOLs were the same model of lens and were explanted from patients, but Lens 4 had crystal deposits while Lens 6 did not. Fig. 3A and B show cross-sections of Lens 4 after milling the lens optic that contained a high density of crystals. The micropores observed when using a razor blade to prepare the sample for imaging (Fig. S3C) were not observed in the subsurface of the lens material after FIB milling. Further 3D image reconstruction from the FIB/SEM did not find micropores in the lens polymer; however, nanopores were observed that overlaid perfectly with the areas of the IOL containing crystals (Fig. 3C and D, Video S1). Performing the same FIB/SEM experiment on Lens 6 did not reveal any micro or nano-sized porous features (Fig. S7) and also showed that FIB milling produced a cleaner cut than with the razor blade. A non-implanted control lens (Lens 7) also did not show any porosity in the material from cross-sectional SEM (Fig. S8).

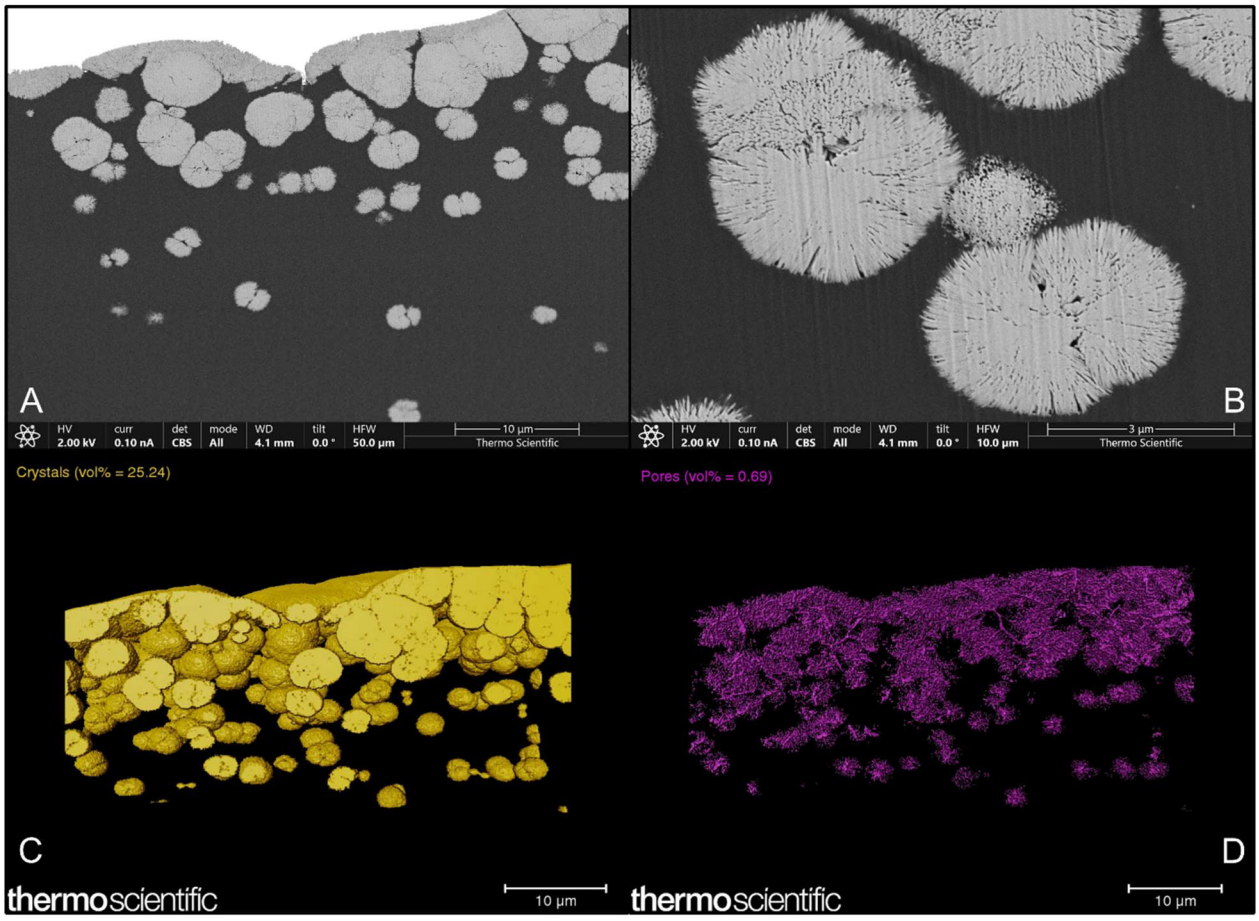

Fig. 3 SEM cross-sectional images of Lens 4 (A) showing that crystals form >30 μm beneath the IOL surface, (B) zoomed view of A showing crystals ranging from 1.5–4 μm in diameter. 3D reconstruction images identifying locations of (C) micro-sized crystals and (D) nano-sized pores. The 3D reconstruction is shown in Video S1.

These results suggest that the porous microchannels observed in our SEM images were not due to manufacturing defects but are likely artifacts of sample preparation from areas that had contained multiple crystals. These crystals were forcefully removed with the razor blade—leaving porous voids behind—but using the FIB to mill the lens produced a cleaner cut that eliminated this artifact. Additionally, FIB/SEM was also beneficial because it provided insight into damage sustained in the IOLs. The images suggest that as crystals grow, nanoporous features are torn into the lens polymer. These structures may enable transport of seed crystals and ions further down into the lens to form new crystals in the subsurface.

Molecular identification of IOL deposits using XRD

Although powder XRD is adept at determining the composition and structure of stochastically oriented crystal samples, the small size and low quantity of crystals on IOLs hinder analysis with a standard powder diffractometer. Only three previous reports published powder XRD data on calcified IOLs, but the resulting powder patterns showed only two peaks with poor signal-to-noise,[11,34,35] which precluded definite identification. Alternatively, electron diffraction using TEM can be used to focus an electron beam directly onto a single IOL crystal. However, broad background signals from the source occlude low-angle diffraction peaks needed to identify the material.[36] Problems with these techniques highlight the need for a method to definitively elucidate the molecular identity of crystals on IOLs.

SCDs have the potential to overcome the issues with other techniques. They can accommodate the small size of IOLs, the low density of crystals on curved surfaces, and can measure low diffraction angles. Thus, an SCD was used to analyze IOL crystals. When first preparing the samples, care was taken to cut away as much of the amorphous lens material as possible to reduce background and enable more selective interrogation of the crystal deposits (Fig. 4A). The sample was adhered to the micromount using oil (Fig. 4B), which held the IOL in place during collection under ambient conditions. Each IOL sample was then analyzed by the SCD. Isotropic Debye–Sherrer rings from the samples (Fig. 4C) were measured with an area detector and integrated using Bruker Apex4 software to obtain 1D powder patterns (Fig. 4D and S1D, S2E, S3D, S4E).

The powder XRD pattern for Lens 1 is presented in Fig. 4D (black trace) along with reference peaks for HAP and OCP from the PDF database. These references are presented for comparison based on previous literature suggesting that IOL crystals are either HAP or OCP.[11,34,36] Comparing the crystalline substance on Lens 1 with references from the database, IOL deposits were identified as HAP. All major peaks from HAP (Fig. 4D, blue) were present on the IOL. By contrast, the three most intense peaks for OCP at 4.72°, 9.44°, and 9.76° (Fig. 4D, green) were entirely absent from the explanted IOL. The abilities of the SCD to measure low diffraction angles from few crystals were key to readily eliminating OCP as the potential material. Results showed that the crystals appear to only contain HAP and not a mixture of other calcium phosphate phases, including OCP, or any other crystalline substances. All optic and/or haptic regions on all five IOLs exhibited identical powder patterns (Fig. 4D and S1D, S2E, S3D, S4E). These results conclusively identify crystals on explanted IOLs as HAP.

However, comparing crystalline deposits on Lens 4 to unsubstituted HAP revealed a shift to higher 2θ values of the (2 1 1), (3 0 0), and (2 0 2) peaks (Fig. 5). These discrepancies indicate that IOL crystal deposits are not stoichiometric HAP ($Ca_{10}(PO_4)_6(OH)_2$) but rather a substituted form. The PDF data-

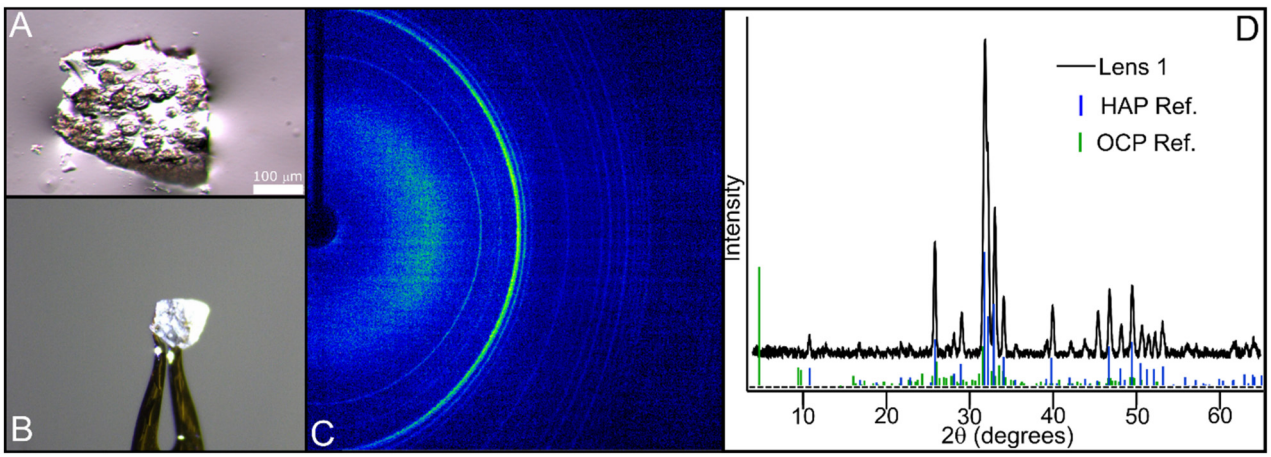

Fig. 4 (A) Micrograph of the piece of Lens 1 used to obtain the diffraction pattern in C. Few crystals were needed on the lens for the measurement. (B) Image of the lens mounted on the single-crystal diffractometer. (C) 2D detector image of the IOL crystal diffraction showing the Debye–Scherrer rings. Green indicates high intensity. The black circle is the outline of the beam stop. The beam stop is 2θ = 0 degrees, and moving radially increases to higher 2θ angles. (D) The integrated 1D powder patterns of Lens 1 (black) compared with the Powder Diffraction Files database for HAP (PDF2 01-071-5048, blue) and OCP (PDF2 00-026-1056, green). The powder patterns were corrected for amorphous background signals as described in the SI (Background signal subtraction for powder XRD of IOLs, Fig. S9).

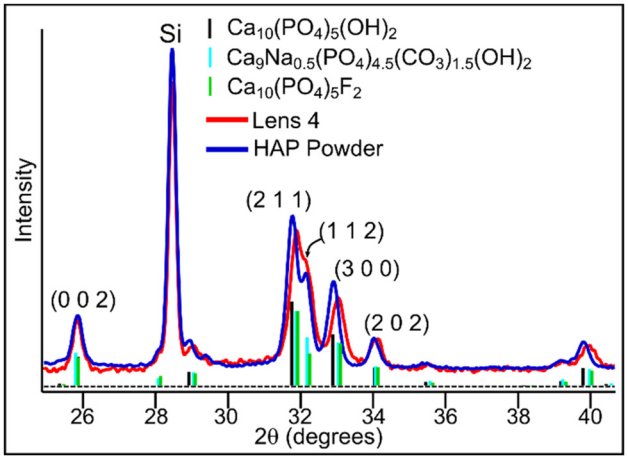

Fig. 5 Comparison of Lens 4 powder pattern (red trace) with the commercial HAP powder pattern (blue trace) collected on the SCD. Si was added to both Lens 4 and HAP as an internal standard (peak at 28.5 degrees). References from the Powder Diffraction Files database are shown for stoichiometric HAP ($Ca_{10}(PO_4)_6(OH)_2$; PDF2 01-071-5048, black), $Ca_9Na_{0.5}(PO_4)_{4.5}(CO_3)_{1.5}(OH_2)$ (PDF2 00-053-0673, light blue), and fluorapatite ($Ca_{10}(PO_4)_6(F)_2$; PDF2 01-080-8486, green).

base was searched to identify potential HAP modifications, two examples of which are presented in Fig. 5 (light blue and green). However, no compounds in the database produced great fits to the IOL crystals. More intricate analytical work was required to verify substitutions in the HAP crystals on the IOLs to confirm the presence of previously unidentified elements, such as Na that was detected in our EDS results.

Elucidating substitutions in IOL crystals

Rietveld refinement (described in the SI: Rietveld Refinement (RR) details) was then performed to compare diffraction patterns of the lens crystals and HAP powder using the single-crystal X-ray structure of stoichiometric HAP as the starting model.[37] Without refining the atomic coordinates, thermal parameters, or atom occupancies, results from our analysis of the HAP powder showed good agreement with the NIST HAP standard (Table 2). However, the lattice parameters changed for the IOL deposits, which indicates that HAP crystals on IOLs have an altered structure. To verify that the lens material and/or shape did not artificially bias the measurement, a lens was coated with the commercial HAP powder and reanalyzed. The lattice parameters matched those of the HAP powder and NIST standard, which proves that the lens does not affect the measurement. These results validate that IOL crystals have a substituted structure compared to stoichiometric HAP. IOL samples were consistently lower for lattice parameter *a*. Previous powder XRD studies reported that a decrease in the unit cell parameter *a* occurs when carbonate exchanges for a phosphate in the HAP structure (called B-type carbonated-HAP, cHAP).[38,39] For comparison, when carbonate exchanges for two hydroxide ions, unit cell parameter *a* increases (called A-type cHAP). This information suggests that IOL crystals possess a carbonate substituted in place of a phosphate. Furthermore, the ratio of *c*/*a* from our XRD measurements supports the assignment of one carbonate per unit cell.[17]

To check for the presence of carbonate or other molecular substitutions in the IOL crystals, Raman microscopy was used to analyze Lens 1. A strong peak was observed at 960 cm^{-1} that was attributed to the $\nu_1(PO_4^{3-})$ peak and a medium peak was present at 1071 cm^{-1} due to $\nu_1(CO_3^{2-})$ (Fig. S10).[39,40] Additionally, the CO_3^{2-} band appeared at 1071 cm^{-1} instead of at 1108 cm^{-1} which indicates that carbonate ions exchanged for phosphate ions in the HAP structure, instead of hydroxide ions.[40,41] This substitution is common in biological organisms, as B-type carbonation is the most common form of cHAP found in bone.[17,40] Mixtures of A-type and B-type HAP are also found in dental enamel, with A-type making up to 10% of the carbonate composition.[40] However, A-type Raman spectra have shown the $\nu_1(PO_4^{3-})$ peak is at 957 cm^{-1} with a distinct shoulder at 947 cm^{-1}.[40] This was not observed in our Raman spectra; thus, our Raman results further supports that carbonate ions exchange for phosphate ions (B-type).

The amount of carbonate incorporation can also be quantified using the intensity ratio of the 1071 cm^{-1} and 960 cm^{-1} peaks.[40,42] Using this I_{1071}/I_{960} ratio from our Raman suggests approximately 6–7% wt/wt of carbonate is incorporated.[42] Our XRD analysis suggested one carbonate per unit cell, which equates to 6.3% for the formula $Ca_{9.5}(PO_4)_5(CO_3)_1(OH)_2$. This is consistent with the Raman intensity ratio result, although half a calcium would be left vacant in the structure to maintain charge balance. Alternatively, given the presence of Na detected by EDS, a Na^+ ion can exchange for a Ca^{2+} ion, providing a formula $Ca_9Na_1(PO_4)_5(CO_3)_1(OH)_2$. This structure is charge balanced and has 6.3% carbonate which fits with our measured result. Thus, both carbonated structures are plausible, as both reconcile with our data. To our knowledge, this is the first report to identify and quantify carbonate in IOL crystal deposits. Previous reports have either reported the deposits as stoichiometric HAP/OCP[11–13] or non-stoichiometric HAP with formula $(Ca_x,Mg_y,Na_z)(PO_4)_3(OH)$ (x, y, and z vary but sum to 5) with a small contamination of Kleemanite ($ZnAl_2(PO_4)_2(OH)_2{\cdot}3H_2O$).[14] Our XRD analysis did not measure

Table 2 Table of the unit cell parameters after Rietveld refinement

Unit cell parameters	Stoichiometric HAP from NIST SRM 2910	HAP powder on powder diffractometer	HAP powder on SCD	HAP powder on IOL on SCD	Crystals on Lens 1	Crystals on Lens 2	Crystals on Lens 4
a (Å)	9.42253(13)	9.42431(13)	9.4227(2)	9.4204(4)	9.3856(3)	9.3830(5)	9.3888(5)
c (Å)	6.88501(9)	6.89626(15)	6.8923(2)	6.8921(5)	6.8919(3)	6.8972(6)	6.8944(5)

any additional crystalline phases and our EDS analysis did not detect Zn. Previous studies using EDS could not measure carbonate due to interfering background signals from the lens material; however, by using XRD and Raman, we were able to identify the crystals as B-type cHAP.

The formula presented based on the XRD and Raman results, $Ca_9Na_1(PO_4)_5(CO_3)_1(OH)_2$, has an appropriate percentage of carbonate (6.3%) and its Ca/Na ratio of 9 falls within the expected range (10 ± 2). However, the Ca/P ratio is 1.8, which is beyond the range of our EDS results (1.51 ± 0.14). This discrepancy suggests that Ca vacancies and/or other ion substitutions may be incorporated into the crystals.[11,12,14] Rational structures were then sought that contained Na and carbonate substitutions while also maintaining constraints imposed by the measured elemental ratios. A formula that best fits these criteria is $Ca_{7.5}Na_{0.7}(PO_4)_{3.5}(HPO_4)_{1.5}(CO_3)_1(OH)_{0.2}$. This structure is similar to that of bone $(Ca_{7.5}(PO_4)_{2.8}(HPO_4)_{2.6}(CO_3)_{0.6}(OH)_{0.2})$[43] and has a Ca/Na ratio of 10, Ca/P of 1.5, and CO_3^{2-} wt/wt of 7.0%, all of which fit the ratios obtained from our EDS and XPS data. However, our Raman data suggested that HPO_4^{2-} ions were not present in the crystals because of the absence of peaks at 1004 cm^{-1}, 916 cm^{-1}, and 878 cm^{-1}.[44] Although both $Ca_9Na_1(PO_4)_5(CO_3)_1(OH)_2$ and $Ca_{7.5}Na_{0.7}(PO_4)_{3.5}(HPO_4)_{1.5}(CO_3)_1(OH)_{0.2}$ are plausible formulas for IOL deposits, neither perfectly matches all the characterization data.

RR was then performed for both proposed structures to assess their fits *versus* the XRD patterns of IOL crystals (described in SI: Structural refinement using Rietveld refinement). The modeled pattern for $Ca_9Na_1(PO_4)_5(CO_3)_1(OH)_2$ aligned well (Fig. 6A). All major peaks were present at similar intensities for the calculated profile, particularly the peaks at 32, 33, and 34° 2θ matched closely to that of the IOL. By contrast, $Ca_{7.5}Na_{0.7}(PO_4)_{3.5}(HPO_4)_{1.5}(CO_3)_1(OH)_{0.2}$ resulted in a poor fit (Fig. 6B). Although the major peaks were present, the peak intensities did not align with the IOL crystals, indicating a problem with the formula. By varying the Ca occupancies, it was evident that the Ca sites needed to be included in the model for these peak intensities to match. Additionally, reducing the number of hydroxide ions caused significant changes in the intensities of several peaks. Although spectroscopic data from EDS and XPS prefer $Ca_{7.5}Na_{0.7}(PO_4)_{3.5}(HPO_4)_{1.5}(CO_3)_1(OH)_{0.2}$ as the assigned structure, this formula cannot be reconciled with the XRD and Raman data.

Considering all the evidence from multiple analytical techniques, we propose that IOL crystals are comprised of $Ca_9Na_1(PO_4)_5(CO_3)_1(OH)_2$ with interspersed amorphous calcium phosphate (ACP). ACP are non-crystalline calcium phosphates that have a Ca/P ratio of 1.36 at pH 7.4.[45] The presence of ACP in IOL crystals would account for the reduced Ca/P ratio measured by EDS and XPS. In a mixture, $Ca_9Na_1(PO_4)_5(CO_3)_1(OH)_2$ contributes a Ca/P of 1.8 while ACP contributes a Ca/P of 1.36. Thus, when combined, the measured ensemble signal converges at our measured Ca/P of 1.51. This explanation reconciles the discrepancy in the elemental spectroscopy results. Furthermore, because ACP is amorphous, it does not appear in XRD patterns; only the crystallized $Ca_9Na_1(PO_4)_5(CO_3)_1(OH)_2$ provides signal. This explains the good XRD fit of the formula with the IOL crystal pattern.

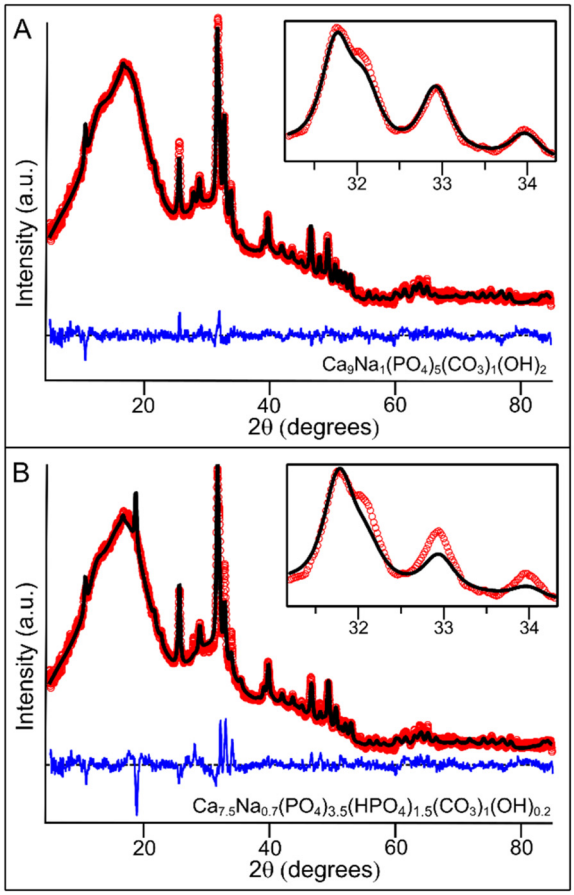

Fig. 6 Rietveld analysis of the Lens 4 powder pattern (red circles) using two proposed crystal structures of substituted HAP structures, (A) $Ca_9Na_1(PO_4)_5(CO_3)_1(OH)_2$ and (B) $Ca_{7.5}Na_{0.7}(PO_4)_{3.5}(HPO_4)_{1.5}(CO_3)_1(OH)_{0.2}$. The calculated patterns are depicted as solid black lines and the difference curves are solid blue lines (offset and centered on a zero line). The inset shows the major diffraction peaks between 31–34° 2θ.

Our proposed structure for IOL crystals is similar to that of bone, and we assert that its formation follows a similar mechanism. Under physiological conditions, ACP is the starting material for the production of cHAP in the bone mineralization pathway.[15,16,46–49] As crystalline cHAP lattices form, an ACP layer is trapped in between units, creating a layered structure.[43,50,51] Although the reported HAP composition of bone differs from IOL deposits, the formation of similar alternating crystalline and amorphous layers rationalizes the results observed from our XRD, EDS, XPS, and Raman analyses. This layered structure also provides a potential explanation for the concentric rings observed in IOL crystals during SEM imaging. Additionally, our proposed chemical formula is consistent with other reports on

the formation of sodiated cHAP, where a coupled substitution of (Na^+ + CO_3^{2-}) takes the place of (Ca^{2+} + PO_4^{3-}). This scheme results in the production of a material with the general formula $Ca_{10-x}Na_x(PO_4)_{6-x}(CO_3)_x(OH)_2$.[52,53] Our proposed $Ca_9Na_1(PO_4)_5(CO_3)_1(OH)_2$ structure for IOL crystals aligns with this formula. Future studies are needed to validate our conclusions by analyzing larger numbers of explanted IOLs with our multi-faceted analyses to robustly characterize the deposits.

Conclusion

This report provides unique insight into the structure and potential mechanism of formation of microscopic IOL deposits. No single analytical technique could sufficiently characterize IOL crystals, so multiple techniques were used to attain complementary information. By combining XRD results with those from EDS, XPS, and Raman, the proposed molecular structure of IOL deposits is crystalline sodiated cHAP ($Ca_9Na(PO_4)_5CO_3(OH)_2$) layered with amorphous ACP. Substituted HAP is prevalent in bone, which indicates that IOL calcification could follow a similar mechanism.

The rarity of crystals on implanted IOLs suggests that relatively few patients possess an ocular microenvironment capable of supporting crystal growth. Clinical studies have shown increased occurrences of IOL calcification when patients undergo additional eye surgeries involving intraocular gas insertion (*e.g.* pars plana vitrectomy, pseudophakic endothelial keratoplasty).[3,4] Altering the microenvironment in the eye with exogenous materials may cause a predisposition to crystal formation, rather than any intrinsic properties of the IOL. This assertion is supported by our FIB/SEM results that did not indicate the presence of any voids in the lens material that could serve as nucleation sites. However, far larger sample sizes are needed to make definitive conclusions. Such studies are encouraged to use FIB/SEM to section the IOL to eliminate artifacts caused by a blade and enable unbiased identification of potential voids.

Similarly, speculations made by other groups that hydrophilic IOL polymers attract calcium and phosphate ions to the lens surface to cause crystal nucleation[11] is not supported by the rarity of IOL deposit occurrence in patients.[2] Crystal formation is most likely caused by "at-risk" ocular microenvironments stimulated by environmental factors. It remains unclear which biomolecular constituents in the microenvironment induce crystal deposition on IOLs, but we assert that similar components are also present during bone growth.[54] Elucidating these connections presents an intriguing area of investigation in future studies.

Author contributions

CLW: conceptualization, visualization, methodology, investigation, formal analysis, data curation, validation, writing – original draft, writing – review & editing; SSP: investigation, formal analysis, data curation, writing – review & editing; ZM: investigation, formal analysis, data curation. BXR: conceptualization, investigation, project administration, writing – original, writing – review & editing; MDAG: investigation, formal analysis, writing – review & editing; MA: investigation, formal analysis; YX: investigation, writing – review & editing; APA: supervision, writing – review & editing; JAW: project administration, visualization, funding acquisition, supervision, writing – review & editing. THL: visualization, writing – original, writing – review & editing. XL: supervision, conceptualization, funding acquisition, project administration.

Conflicts of interest

There are no conflicts of interest to declare.

Data availability

The data supporting this article has been included in the manuscript and in the supplementary information (SI). Supplementary information: additional micrographs, SEM images, EDS results, and powder XRD patterns for Lenses 2–7. Also included: video of FIB/SEM 3D reconstruction of Lens 4, a table of the XPS results, image of the Raman spectrum, and all the details for processing and analyzing the powder XRD patterns (PDF). See DOI: https://doi.org/10.1039/d5an00999e.

Acknowledgements

Funding for this study was provided by a Research to Prevent Blindness grant awarded to the Kresge Eye Institute at Wayne State University. This work made use of the single-crystal XRD partially funded by the National Institutes of Health #3R01EB027103-02S1, the XPS partially funded by National Science Foundation #1849578, and the SEM funded by the National Science Foundation #0922912. The authors would like to thank Thermo Fisher Scientific for conducting FIB/SEM imaging.

References

1 D. J. Apple and L. Werner, *Trans. Am. Ophthalmol. Soc.*, 2001, **99**, 95–107.
2 A. Grzybowski, G. U. Auffarth and B. R. LaHood, *Curr. Opin. Ophthalmol.*, 2025, **36**, 18–24.
3 B. Memmi, J. Knoeri, N. Bouheraoua and V. Borderie, *Am. J. Ophthalmol.*, 2023, **246**, 86–95.
4 S. Bopp, H. B. Özdemir, Z. Aktaş, R. Khoramnia, T. M. Yildirim, S. Schickhardt, G. U. Auffarth and Ş. Özdek, *Diagnostics*, 2023, **13**, 1943–1956.
5 D. A. Märker, V. Radeck, T. Barth, H. Helbig and N. C. Scherer, *Clin. Ophthalmol.*, 2023, **17**, 3243–3248.

6 I. M. Neuhann, G. Kleinmann and D. J. Apple, *Ophthalmology*, 2008, **115**, 73–79.
7 M. W. Dorey, S. Brownstein, V. E. Hill, B. Mathew, G. Botton, P. J. Kertes and S. El-Defrawy, *Am. J. Ophthalmol.*, 2003, **135**, 591–598.
8 R. Mukherjee, K. Chaudhury, S. Das, S. Sengupta and P. Biswas, *Micron*, 2012, **43**, 937–947.
9 L. Werner, *J. Cataract Refractive Surg.*, 2007, **33**, 713–726.
10 D. Tognetto, L. Toto, E. Ballone and G. Ravalico, *J. Cataract Refractive Surg.*, 2002, **28**, 644–651.
11 S. P. Gartaganis, D. G. Kanellopoulou, E. K. Mela, V. S. Panteli and P. G. Koutsoukos, *Am. J. Ophthalmol.*, 2008, **146**, 395–403.
12 S. P. Gartaganis, P. Prahs, E. D. Lazari, P. S. Gartaganis, H. Helbig and P. G. Koutsoukos, *Am. J. Ophthalmol.*, 2016, **168**, 68–77.
13 E. G. Drimtzias, S. G. Rokidi, S. P. Gartaganis and P. G. Koutsoukos, *Am. J. Ophthalmol.*, 2011, **152**, 824–833.
14 S. E. Avetisov, A. A. Gamidov, I. A. Novikov, A. A. Fedorov and A. A. Kas'yanov, *Vestn. Oftalmol.*, 2015, **131**, 74–78.
15 M. S. Tung and W. E. Brown, *Calcif. Tissue Int.*, 1983, **35**, 783–790.
16 W. Pompe, H. Worch, W. J. E. M. Habraken, P. Simon, R. Kniep, H. Ehrlich and P. Paufler, *J. Mater. Chem. B*, 2015, **3**, 5318–5329.
17 E. Landi, G. Celotti, G. Logroscino and A. Tampieri, *J. Eur. Ceram. Soc.*, 2003, **23**, 2931–2937.
18 P. Grøn, *Arch. Oral Biol.*, 1973, **18**, 1385–1392.
19 Q. Liu, Y. Luo, Y. Zhao, P. Xiang, J. Zhu, W. Jing, W. Jin, M. Chen, R. Tang and H. Yu, *Bioact. Mater.*, 2022, **8**, 478–493.
20 B. Xie, T. J. Halter, B. M. Borah and G. H. Nancollas, *Cryst. Growth Des.*, 2015, **15**, 204–211.
21 R. B. Thompson, V. Reffatto, J. G. Bundy, E. Kortvely, J. M. Flinn, A. Lanzirotti, E. A. Jones, D. S. McPhail, S. Fearn, K. Boldt, M. Ueffing, S. G. S. Ratu, L. Pauleikhoff, A. C. Bird and I. Lengyel, *Proc. Natl. Acad. Sci. U. S. A.*, 2015, **112**, 1565–1570.
22 A. Dhital, D. J. Spalton, S. Goyal and L. Werner, *Am. J. Ophthalmol.*, 2012, **153**, 1154–1160.
23 P. Kanclerz, T. M. Yildirim and R. Khoramnia, *Arch. Pathol. Lab. Med.*, 2020, **145**, 759–767.
24 A. M. Izak, L. Werner, S. K. Pandey and D. J. Apple, *Eye*, 2003, **17**, 393–406.
25 I. Kovrlija, J. Locs and D. Loca, *Acta Biomater.*, 2021, **135**, 27–47.
26 C. C. Chusuei, D. W. Goodman, M. J. Van Stipdonk, D. R. Justes and E. A. Schweikert, *Anal. Chem.*, 1999, **71**, 149–153.
27 J. A. Small, *J. Res. Natl. Inst. Stand. Technol.*, 2002, **107**, 555–566.
28 T. L. Barr and S. Seal, *J. Vac. Sci. Technol., A*, 1995, **13**, 1239–1246.
29 N. Fairley, V. Fernandez, M. Richard-Plouet, C. Guillot-Deudon, J. Walton, E. Smith, D. Flahaut, M. Greiner, M. Biesinger, S. Tougaard, D. Morgan and J. Baltrusaitis, *Appl. Surf. Sci. Adv.*, 2021, **5**, 100112.
30 K. Darcy, A. Apel, M. Donaldson, R. McDonald, J. Males, M. Coote, L. Werner and E. Chan, *Br. J. Ophthalmol.*, 2019, **103**, 1700–1703.
31 F. A. Shah, K. Ruscsák and A. Palmquist, *Bone Res.*, 2019, **7**, 15–29.
32 H. Nabika, M. Itatani and I. Lagzi, *Langmuir*, 2020, **36**, 481–497.
33 H. Kim, G. Holló, C. M. Heo, I. Lagzi, H. Lee and S. H. Yang, *Cryst. Growth Des.*, 2024, **24**, 8794–8802.
34 P. G. Koutsoukos, P. D. Natsi, S. P. Gartaganis and P. S. Gartaganis, *Crystals*, 2022, **12**, 1418–1437.
35 A. K. F. Yu and T. W. H. Shek, *Arch. Ophthalmol.*, 2001, **119**, 611–614.
36 L. Britz, S. K. Schickhardt, T. M. Yildirim, G. U. Auffarth, I. Lieberwirth and R. Khoramnia, *Sci. Rep.*, 2022, **12**, 7685–7694.
37 K. Sudarsanan and R. A. Young, *Acta Crystallogr., Sect. B*, 1969, **25**, 1534–1543.
38 K. Sugimoto, Y. Zhou, T. G. Galindo, R. Kimura and M. Tagaya, *Biomimetics*, 2023, **8**, 184–198.
39 A. Krajewski, M. Mazzocchi, P. L. Buldini, A. Ravaglioli, A. Tinti, P. Taddei and C. Fagnano, *J. Mol. Struct.*, 2005, **744–747**, 221–228.
40 G. Penel, G. Leroy, C. Rey and E. Bres, *Calcif. Tissue Int.*, 1998, **63**, 475–481.
41 R. M. Wilson, J. C. Elliott, S. E. P. Dowker and L. M. Rodriguez-Lorenzo, *Biomaterials*, 2005, **26**, 1317–1327.
42 A. Awonusi, M. D. Morris and M. M. J. Tecklenburg, *Calcif. Tissue Int.*, 2007, **81**, 46–52.
43 S. Von Euw, Y. Wang, G. Laurent, C. Drouet, F. Babonneau, N. Nassif and T. Azaïs, *Sci. Rep.*, 2019, **9**, 8456–8466.
44 B. O. Fowler, M. Markovic and W. E. Brown, *Chem. Mater.*, 1993, **5**, 1417–1423.
45 J. D. Termine and E. D. Eanes, *Calcif. Tissue Res.*, 1972, **10**, 171–197.
46 J. Mahamid, A. Sharir, L. Addadi and S. Weiner, *Proc. Natl. Acad. Sci. U. S. A.*, 2008, **105**, 12748–12753.
47 F. Nudelman, K. Pieterse, A. George, P. H. H. Bomans, H. Friedrich, L. J. Brylka, P. A. J. Hilbers, G. de With and N. A. J. M. Sommerdijk, *Nat. Mater.*, 2010, **9**, 1004–1009.
48 D. G. A. Nelson and J. C. Barry, *Anat. Rec.*, 1989, **224**, 265–276.
49 A. Lotsari, A. K. Rajasekharan, M. Halvarsson and M. Andersson, *Nat. Commun.*, 2018, **9**, 4170–4180.
50 Y.-H. Tseng, C.-Y. Mou and J. C. C. Chan, *J. Am. Chem. Soc.*, 2006, **128**, 6909–6918.
51 W. E. Brown, J. P. Smith, J. R. Lehr and A. W. Frazier, *Nature*, 1962, **196**, 1050–1055.
52 E. A. P. De Maeyer and R. M. H. Verbeeck, *Bull. Soc. Chim. Belg.*, 1993, **102**, 601–609.
53 N. S. Chickerur, M. S. Tung and W. E. Brown, *Calcif. Tissue Int.*, 1980, **32**, 55–62.
54 A. George and A. Veis, *Chem. Rev.*, 2008, **108**, 4670–4693.